小鼠杏仁核中央核側區神經細胞之電位控制型鉀離子通道特性研究

Characterization of Voltage-gated K^+ Channels in Lateral Subdivision of Central Amygdala Neurons

研究生：郭寧（Ning Kuo）

指導教授：連正章 博士（Cheng-Chang Lien, M.D., Ph.D.）

國立陽明大學

神經科學研究所

碩士論文

Institute of Neuroscience

National Yang-Ming University

Master Thesis

中華民國一百零三年七月

July, 2014

致謝

本論文得以順利完成，要感謝許多人的支持與幫助。首先，感謝指導教授 連正章老師，給予我電生理實驗訓練，並且不遺餘力教學指導研究知識。此外十分感謝口試委員 孫興祥老師，曹美玲老師以及鄭菡若老師對本論文的指導與建議，讓我得以更多面且嚴謹審視此研究成果。也要感謝陽明大學神經科學研究所，給予我機會進入神經科學知識的領域。

感謝實驗室的各位，柏翰，僕射，晏竹，筑方，在我不熟悉實驗室的時候耐心教導我，並在實驗操作和背景知識上給予我幫助。感謝文賢也提供了部分研究資料，並和我討論研究的方向。感謝茵絪在免疫螢光染色上的指導與幫忙，提供了我研究的廣度。此外，感謝實驗室其他成員們，儒韻，于超，思懿，燦庭，政達，至緯，建錞，亭伃，廷耘，玠如，敏華和昱伶，在實驗和生活上幫助我，豐富我實驗室生活的色彩。

感謝一路陪我走來的好友們，給我支持也一起分享喜悅和悲傷。最後感謝愛我的家人們，總是關心我，支持我，為我著想，給予我力量。

謹以此論文獻給我的家人，朋友們，謝謝你們。

郭寧 謹致於

國立陽明大學神經科學研究所

中華民國一百零三年七月

Table of contents

中文摘要

杏仁核在情緒表現以及恐懼記憶制約學習方面扮演重要角色，此構造能再細分為各個區域，包括基底核、外側核、中央核以及中間聯絡神經元細胞層等。其中，中央核能再以結構及功能分成外側區與內側區。先前的研究已指出中央核外側區內的神經元主要為分泌伽瑪胺基丁酸的神經元，且此結構在功能上能調控恐懼行為的表現，因此中央核外側區被認為是表現恐懼行為記憶的關鍵區域。依據全細胞紀錄的結果，我們在杏仁核中央核外側區的神經元上能記錄到彼此相異的動作電位模式和細胞特性，並得以依此將杏仁核中央核外側區的細胞粗略分為至少兩群：一類有著緩慢坡升的去極化過程，以及延遲產生的動作電位；另一類則是較快產生動作電位。

以現有的知識來推測造成此區別的機制能聯想到兩種可能，一是其細胞型態的影響，另一方面則是神經元上所表現的離子通道作用，得以塑造出動作電位的不同型態與模式。其中電位控制型鉀離子通道的開關過程能塑造動作電位的寬度與產生時間，因此電位控制型鉀離子通道的表現也被認為是決定不同神經細胞之間動作電位模式差異的重要因素。我們主要專注於功能性電位控制型鉀離子通道在杏仁核中央核外側區的特性研究，實驗指出，當以藥物抑制第一型電位控制型鉀離子通道時，能夠使延遲產生動作電位的神經元提前產生動作電位，其動作電位的特性也較接近另一種較快產生動作電位的神經元所展現的特性，而抑制第一型電位控制型鉀離子通道對於原本能較快產生動作電位的神經元則沒有顯著的影響。顯示第一型電位控制型鉀離子通道參與控制中央核外側區神經元動作電位的產生時間，使其中一類杏仁核中央核外側區神經元延遲產生動作電位。但在另一方面，測量細胞本體的細胞膜上的電位控制型鉀離子通道電流並研究其特性時，除了 A 型鉀離子電流的衰退時間之外，並未發現在此兩群細胞本體的電位控制型鉀離子通道有電生理特性或是單元組成的顯著差異。這暗示我們，第一型電位控

制型鉀離子通道的在杏仁核中央核外側區的主要差異可能並不是在神經細胞本體的細胞膜上體現。免疫螢光染色的結果也顯示，第一型電位控制型鉀離子通道的螢光訊號沒有與軸突起始段標誌蛋白的訊號共同分布在細胞的同一區域，推定第一型電位控制型鉀離子通道可能也並未表現於軸突起始段。

Abstract

The amygdala is a key brain structure involved in emotional processing, conditioned fear learning and memory. The amygdala can be divided into different subregions, including basal amygdala (BA), lateral amygdala (LA), the central nucleus of the amygdala (CeA) and intercalated cell masses (ICMs). The CeA can be further divided into the lateral part (CeL) and medial part (CeM). The majority of neurons in the CeL, considered to regulate the expression of fear expression, are GABAergic neurons. Using whole-cell recordings, we found that CeL neurons display diverse firing patterns and intrinsic properties. These neurons were classified based on their electrophysiology properties. At least, two major types of neurons were identified in the CeL; late-spiking (LS) neurons exhibit a slow ramping depolarization phenotype and longer spike latency compared to early-spiking (ES) neurons.

It is known that firing pattern of a given neuron is determined by the morphological architecture and a repertoire of intrinsic membrane conductances. Since activation and inactivation of voltage-gated potassium (K_v) channels can shape the spike waveform and spike precision, their expression is one of the main factors in determining the firing phenotypes. The specific aim of this study is to characterize the functional properties of K_v channels in CeL cells. Application of a potassium channel blockers 4-aminopyramidine (4-AP) at a low concentration (30 μM) and α-dendrotoxin (α-DTX; 100 nM) can reduced the spike delay of LS neurons but had little effect on ES neurons. The result indicates that 4-AP- and α-DTX-sensitive, K_v1-like K^+ current plays an important role in mediating the spike delay, thus defining the firing pattern of CeL neurons. While in nucleated patch recordings, no significant difference of somatic K_v channels properties or subtype composition were found

between both types of CeL neurons, except in the decay time of A-type K^+ current. This result suggests that the major difference in the expression of 4-AP- and α-DTX-sensitive K^+ channels between LS and ES cells is not located primarily on the soma. Further, immunohistochemical staining of the axon initial segment (AIS) marker Ankyrin-G (Ank-G) and K_v1 channels showed that K_v1 channels did not co-localized with Ank-G, suggesting that the K_v1 channels are not expressed on the AIS.

Abbreviations

4-AP, 4-amino-pyridine

aCSF, artificial cerebrospinal fluid

AIS, axon initial segment

Ank-G, Ankyrin-G

BLA, basolateral nucleus of the amygdala

CeA, central nucleus of the amygdala

CeL, lateral division of the central nucleus of the amygdala

α-DTX, α-dendrotoxin

ES cell, early-spiking cell

LS cell, late-spiking cell

LTB cell, low-threshold bursting cell

ICM, intercalated cell mass

K_v channel, voltage-gated potassium channel

TEA, tetraethylammonium

TTX, tetrodotoxin

Introduction

The amygdala

The amygdala is a complex structure in the medial temporal lobe region that plays a key role in emotional learning and fear conditioning (LeDoux, 2007; Ehrlich et al., 2009; Johansen et al., 2011). The amygdala can be separated to several defined nuclei, including the basolateral nucleus of the amygdala (BLA), the central nucleus of the amygdala (CeA), and intercalated cell masses (ICMs). The key circuits mediating fear conditioning in mammals consist of conditional stimulus (CS) and unconditional stimulus (US) that converge onto single neurons in the lateral nucleus of the amygdala (LA). The LA projects to the CeA both directly and indirectly by way of connections in other amygdala regions (Pitkänen et al., 1997; Amano et al., 2010; Johansen et al., 2011). The CeA, thought to control the expression of fear behavior, can be further divided into the lateral (CeL) and medial (CeM) subdivisions. The CeM is viewed as the major output station of the amygdala. The CeM outputs drive the expression of conditioned fear responses including freezing behavior and physiological parameters via projections to the brainstem and hypothalamus (Viviani et al., 2011) while CeL neurons innervate the downstream CeM. Thus the CeL is considered to "gate" the expression of fear.

CeL neurons

Most CeL neurons were γ-aminobutyric acid-releasing (GABAergic) inhibitory neurons (Ehrlich et al., 2009), thus the CeL provides tonic inhibition to the CeM and could gate the expression of fear behavior. According to previous studies from different species, the CeL is composed of different populations of GABAergic neurons

categorized by their diverse intrinsic firing properties (Lopez De Armentia and Sah, 2004; Ciocchi et al., 2010; Haubensak et al., 2010; Amano et al., 2012; Li et al., 2013). The role of variant firing phenotypes of CeL neurons is not well-known. It requires investigating CeL neurons at the cellular level.

Mechanisms underlying firing phenotypes

Upon sustained current injection, neurons generate action potentials. Firing patterns of a given neuron is determined by the morphological architecture (Mainen and Sejnowski, 1996) and a repertoire of intrinsic membrane conductances (Hodgkin and Huxley, 1952). The complexity of intrinsic conductances of a given neuron is the basic mechanism underlying the excitability of a given neuron. Sodium currents determine the depolarization speed and height of action potential spikes, while the delayed outward potassium currents result in spike repolarization and shape the width and spiking timing of action potential.

Voltage-gated potassium (K_v) channels

While observing the variant firing properties of the CeL neurons, we want to address that what would make these neurons exhibit different firing pattern. It is known that voltage-gated potassium (K_v) channels play an important role in determining firing patterns of neurons and would further participate in synaptic integration (Lien and Jonas 2003; Hu et al., 2010; Alle et al., 2011). K_v channels, with a voltage-sensor in the units, would activate upon voltage change, thus K_v channels have the ability to influence membrane excitability. As a result, activation of K_v channels can shape the spike waveform and spike precision, thus expression of K_v channels is one of the main factors in determining the variance of firing patterns. For example, K_v3 channels

involve in high-frequency, repetitively firing (Lien et al., 2003), while some delayed-rectifier potassium channels involved in the delayed spike latency. In previous studies, the slowly inactivating, highly 4-AP-sensitive potassium current I_D could cause delay in onset of firing in response to long-lasting depolarizing stimuli (Storm, 1988, Kirchheim et al., 2013). These findings provide a direction for investigating the mechanism of the variant firing patterns of CeL cells.

Specific aim

Since the K_v channel expression profile is unclear in the amygdala CeL, this study aims to investigate the ionic basis underlying the variant firing patterns of CeL neurons, and to reveal how K_v channels are expressed and how they function in CeL neurons.

Materials and methods

Acute amygdale slice preparation

Acute brain slices containing amygdala CeL region were prepared from wild-type C57BL/6 mice of both genders (postnatal 21-45 days) using a commercial vibratome (DTK-1000, Dosaka). Mice were anesthetized with isoflurane, the brains were instantly removed, and the 300 μm thick slices were coronally sectioned in oxygenated (95% O_2/ 5% CO_2) ice-cold cutting solution containing (in mM) 87 NaCl, 25 $NaHCO_3$, 1.25 NaH_2PO_4, 2.5 KCl, 10 glucose, 75 sucrose, 0.5 $CaCl_2$ and 7 $MgCl_2$ and incubated in the same solution in a holding chamber at 34℃ for 30 minutes. Afterwards slices were stored at room temperature until used.

Chemicals and solutions

During experiments, slices were perfused with physiological extracellular solution (artificial cerebrospinal fluid; aCSF) containing (in mM) 125 NaCl, 25 $NaHCO_3$, 1.25 NaH_2PO_4, 2.5 KCl, 25 glucose, 2 $CaCl_2$ and 1 $MgCl_2$. In some whole-cell recording experiments, 2 mM kynurenic acid (Sigma-Alderich) and 1 μM SR95531 (Tocris) were added into the aCSF to block synaptic transmission. In nucleated patch recordings, 0.5-1 μM tetrodotoxin (TTX; Abcam) was added to the external solution to block sodium currents; K_v channel blockers 4-amino-pyridine (4-AP; Sigma-Alderich) and tetraethylammonium (TEA; Sigma-Alderich) were applied to block certain types of K_v channels, depending on the concentration. We also applied α-dendrotoxin (α-DTX; Alomone Labs), in the presence of synaptic blockers and 0.5% bovine serum albumin (BSA; UniRegion Bio-Tech) to block selected K_v1 channels. Recording electrodes were filled intracellular solutions containing (in mM) 135 K-gluconate, 5 EGTA, 10

HEPES, 4 Na_2ATP, 0.5 $CaCl_2$, 2 $MgCl_2$.

Electrophysiology

Recordings were performed in an Axopatch 200B amplifier (Molecular Devices). Recording electrodes (5-15 MΩ) were pulled from borosilicate glass (outer diameter, 1.5 mm; thickness, 0.32 mm; Harvard apparatus). The diameters of the recording pipettes are slightly larger (~3 MΩ) while performing nucleated patches. Signals were low-pass filtered at 5 kHz and sampled at 10 kHz using Digidata 1440A (Molecular Devices). Pulse sequences were generated by Digidata 1440A via pClamp (Molecular Devices). For whole-cell patch-clamp recordings, series resistances were compensated. For nucleated patch recordings, patches were held at -90 mV. Leakage currents were subtracted on-line using a 'P over 4' procedure (Martina et al., 1998; Lien et al., 2002). All recordings were made at room temperature.

K_v current recordings

The K^+ current measurement are made from nucleated patches and whole-cell recordings. Nucleated patches were pulled from CeL neurons. The following steps for making nucleated patches were, as in conventional outside-out patches, obtaining whole-cell recording configuration, then carefully withdrawing the recording pipette from the cell with negative pressure application via suction through the patch pipette, and slowly isolating their somatic membrane to form a sphere (Hamill et al. 1981; Sather et. al. 1991). The data was discarded if the leak current of the patch was larger than -10 pA.

Nucleated patches were held at -90 mV to make K_v channels ready to open. Voltage-clamp protocol consisted of voltage-step commands that jump to + 90 mV or

+70 mV from the holding potential. We isolated A-type and delayed-rectifier K_v channels using pharmacological blockers: the currents remained in the present of 20 mM TEA were TEA-resistant K_v4 currents; and by subtraction of the control current ($I_{control}$, the K^+ current obtained in the presence of TTX) and TEA-resistant K^+ current (I_A), we obtained the delayed-rectifier K^+ current (I_{DR}).

Morphological reconstructions

Morphological reconstructions were done by *post hoc* staining and the software Neuromantic 1.6.3 (Myatt et al., 2012) for more detailed morphological analysis. The biocytin-filled cells were stained with Alexa-594 conjugated with streptavidin or FITC conjugated with avidin, and were scanned by two-photon microscopy. Once the high-resolution two-photon images of CeL were acquired, the morphologies of the cells were reconstructed from the stacks (about 100 images per cell) that ware imported into Neuromantic 1.6.3.

Sholl analysis

Sholl analysis (Sholl, 1953) was performed to check dendritic properties and complexity in relation to their distance from the soma of CeL cells. The concentric Sholl segments with radial interval of 5 μm were generated starting at a distance of 10 μm from the cell center. Quantification of the intersections of concentric circles and dendrite-like processes would reveal the branched levels of the cells. All analyzed data were obtained by the Neurolucida Explorer software (version 10.40 64-bit; MicroBrightField).

K_v currents analysis

Potassium current amplitudes were measured by the peak value during the depolarizing pulse. The value peak current must be three times larger than the standard deviation of baseline mean. To obtain the activation curve, values of K_v conductance were calculated from the respective peak currents, assuming ohmic behavior and a reversal potential of -107 mV. Theoretical reversal potential (E_{rev}) K^+ current was calculated by the Nernst equation:

$$E_{rev} = \frac{RT}{ZF} \ln\left(\frac{[X]_{out}}{[X]_{in}}\right)$$

; where R, T, and F present their standard thermodynamic meanings; $[X]_{out}$ and $[X]_{in}$ are outer and inner K^+ concentrations.

The data points of A-type K_v currents were fitted with Boltzmann functions raised to the forth power for the activation curves:

$$f = \frac{1}{(1 + \exp(\frac{-(v - v_{1/2})}{k}))^4}$$

; where V is the membrane potential, $V_{1/2}$ is the potential where the value of the Boltzmann function will be 0.5, and k is the slope factor. The midpoint potentials (midpoint V) indicate the potential at which f = 0.5. The rise times of the A-type potassium current (K_A) and delayed-rectifier potassium current (K_{DR}) were obtained by calculating the time from 20% to 80% of the peak amplitude. The decay time of the K_A was fitted with the equation:

$$f(t) = A(\exp(-t/t_{decay}))+C$$

; where A is the fraction of inactivating current and C represents the amplitude of remaining current. We could also measure the K^+ current densities: the value of the peak current amplitude was divided by the measured surface area to calculated current densities. It was assumed that the patches were approximately oval shape, and then the surface area was calculated using the following formula:

$$\text{Surface area} = (\text{major axis} + \text{minor axis})^2(\pi/4)$$

Immunohistochemistry staining

(Note: this work was done by Yin-Yin Tsao)

Wild-type mice transcardial perfused using iced filtered 4% paraformaldehyde (PFA) in PBS (pH 7.4) under deep anesthesia by isoflurane inhalation, and the brains removed. The brain tissues were fixed in 4% PFA for 1.5 hours, then transferred to 30% sucrose in PBS for 24 hours, and transferred to fresh 30% sucrose solution for another 24 hours; the dehydration process was performed on shakers. The 20-μm thick mice brain slices were horizontally cryostat sectioned by sliding microtome Leica SM2010R (Leica Biosystms).

The slides were shaken in LTBS for 10 minutes, then transferred to LTBST (0.1% Triton X-100 in LTBS), shook for 10 minutes twice. Then the slides were quenched by LTBST with 0.03% endogenous peroxidase, and shook for 10 minutes twice. Before applying primary antibodies, the slides were washed in LTBST for 10 minutes and blocked using LTBST with 2% BSA and 6% normal goat serum (NGS). For colocalization of K_v1 channels at the AIS of CeL cells, we used monoclonal anti-$K_v1.1$, anti-$K_v1.2$, anti-$K_v1.6$ (Alonmone Labs) and mouse anti-Ankyrin-G (anti-Ank-G; NeuroMab). The slides were incubated overnight in antibodies of K_v1 channels (1:100)

and Ank-G (1:200) within LTBS containing 0.1% Triton-X and 3% NGS. After incubated in the primary antibodies, the slides were rinsed in HTBST (0.1% Triton X-100 in HTBS) and then transferred into secondary antibody solution: LTBST with 6% NGS and secondary antibodies (1:500), protected from light. When the application finished, the slides were washed and mounted for imaging and analysis.

Data analysis and statistics

Data were analyzed using Clampfit 10.2 (Molecular Devices) and Prism 5.0 (GraphPad). Data sets were presented as mean ± standard error of mean (SEM). Statistical significance was examined by the non-parametric t-test using Prism 5.0. Traces in the figures were single or averages of 5 sweeps. Statistical significance was tested by Wicoxon signed-rank at the significance level as indicated.

Results

Firing patterns of CeL neurons

In the current-clamp configuration, CeL neurons exhibit different firing phenotypes in response to 2-second current pulse injection. We distinguished CeL neurons by their spike latency, which is measured from the start of current injection to the time when the spike amplitude reaches to its peak value. If the neurons generated action potentials at 1.5 second or latter after the onset of current pulse injection onset, we defined these cells as late-spiking (LS) neurons otherwise non-LS neurons. Non-LS neurons include early-spiking (ES) neurons and low-threshold bursting (LTB) neurons. LTB neurons exhibited bursting spikes or rebound firing after hyperpolarizing current pulse injection (**Fig. 1A**). The major neuron type was LS neuron (62.6%); the second major type was ES neuron (35.4%), and the LTB accounted for about 3 % (**Fig. 1B**).

Spike latency was measured in the spike generated upon the rheobase, the minimum current pulse injected through the somatic patch pipette for a neuron to generate action potential spikes in the current-clamp configuration. We analyzed the depolarizing responses in CeL neurons and defined the ramp ratio. The ramp ratio was defined as the ratio of voltage responses of certain period a and b, as the given neuron is injected with the current 1 pA smaller than the rheobase so that it would not generate action potential. Period a is the time period of 200 to 250 ms after the onset of current injection, while period b is the time period of 150 ms to 200 ms before the end of current injection. We obtained the value of the ramp ratio by dividing the mean value of the response during period b by the mean value of period a (**Fig. 2A**). We observed that LS cells had a slow ramping depolarization while ES cells did not, and found that

the ramp ratio of most ES neurons was smaller than 1, while LS neurons had larger ramp ratio (**Fig. 2A-D**). We concluded that LS neurons showed a subthreshold ramp phenotype and long spike latency.

Intrinsic properties

In addition to the above mentioned features, there are other differences between LS and ES neurons. There is a significant difference of resting membrane potential (RMP) between LS and ES neurons. LS neurons had a more hyperpolarized RMP than that of ES neurons (LS cells, -70.26 ± 0.54 mV, n = 92, vs. ES cells, -66.35 ± 0.68 mV, n = 51; $P < 0.0001$; Mann Whitney test; F**ig. 3A**). LS and ES neurons also differed in the rheobase (LS cells, 41.79 ± 1.30 pA, n = 92, vs. ES cells, 35.79 ± 2.48 pA, n = 51; $P = 0.005$; Mann Whitney test; **Fig. 3B**). The voltage threshold was defined as dV/dt = 10 mV/ms. However, there was no significant difference between LS and ES cells in AP threshold (data not shown).

Morphological reconstruction of CeL neurons

The LS cells and ES cells both exhibited processes of ~100 μm from soma, and have fewer processes which extend to 300 μm or longer. We cannot distinguish CeL neurons simply by their morphologies (**Fig. 4A**). Sholl analysis revealed that these two groups of CeL cells have similar number of intersections with 100 μm from soma, and the result showed that the dendritic compartments are similar in LS and ES neurons (**Fig. 4 B-D**).

4-AP at low concentrations reduced the spike latency of LS neurons

Previous studies show that 4-AP sensitive conductance plays an important role in determining spike delay (Chieng et. al., 2006). K_v1 channels likely contribute to the prominent delay of LS cells. K_v1 channels are sensitive to low concentration 4-AP, and the specific blocker α-dendrotoxin (α-DTX). To investigate the effect of K_v1 channels on the firing latency of CeL neurons, a low concentration (30 μM) of 4-AP was applied. At this concentration, 4-AP blocks $K_v1.1$, $K_v1.2$, $K_v1.3$, $K_v1.5$, $K_v3.3$ and $K_v3.4$. Application of 4-AP (30 μM) greatly reduced the spike latency (control, 1874 ± 34 ms; 4-AP, 993 ± 103 ms, n=13; $P < 0.01$; Wilcoxon signed-rank test; **Fig. 5A**, top) and the ramp ratio (control, 1.45 ± 0.05; 4-AP, 1.15 ± 0.05, n = 13; $P < 0.01$, Wilcoxon signed-rank test) in LS neurons; However, there was no significant effect on the spike delay (control, 411 ± 129 ms; 4-AP, 412 ± 134 ms, n = 7; P = 0.81; Wilcoxon signed-rank test; **Fig. 5A**, bottom) and ramp ratio (control, 1.00 ± 0.07; 4-AP, 0.92 ± 0.12, n = 7; P = 0.58, Wilcoxon signed-rank test) of ES neurons. The rheobase was also reduced by 30 μM 4-AP in both LS and ES cells. Similarly, α-DTX (100 nM) also preferentially decreased the latency of LS cells (control, 1845 ± 40 ; α-DTX, 1306 ± 149, n= 9; $P < 0.01$, Wilcoxon signed-rank test), but not that of ES cells (control, 645 ± 249 ; α-DTX, 706 ± 168, n = 4; P = 1.00, Wilcoxon signed-rank test). Also, α-DTX decreased the ramp ratio in LS cells (control, 1.36 ± 0.06; α-DTX, 1.22 ± 0.05, n=9; P = 0.019, Wilcoxon signed-rank test; **Fig. 6A**, top), but not in ES cells (control, 0.98 ± 0.12; α-DTX, 1.18 ± 0.12 , n = 4; P = 0.625, Wilcoxon signed-rank test; **Fig. 6A**, bottom). This result indicates that the K_v1-like blockade converted the delay-and-ramp depolarizing pattern of LS cells into ES cell-like phenotype.

Dose-response curves of K_v channel blockers

To address how K_v channels are expressed in CeL neurons, we examined the effect of

K_v channel blockers on K_v currents of CeL neurons. The inhibition of peak and sustained currents by TEA and 4-AP revealed that LS and ES neurons showed similar sensitivities to K_v channel blockers (**Fig. 7 and 8**). Although application of 4-AP (30 μM) markedly decreased the firing latency of LS cells, 4-AP (30 μM) had little effect on the somatic currents in both LS and ES cells (**Fig. 7 and 8**).

LS and ES neurons showed similar K_v channel properties

To investigate K_v channel conductance in CeL neurons, we measured K_v currents in nucleated patches from LS and ES neurons. The activation curve of A-type K_v currents obtained in nucleated patches from LS cells was similar to that in ES cells (slope factor: LS cell, 25.63 ± 0.92, n = 9 vs. ES cell, 25.54 ± 0.87, n = 6; P = 0.61; Mann Whitney test; $V_{1/2}$: LS cell, 2.226 ± 3.356, n = 9 vs. ES cell, 10.36 ± 2.727, n = 6; P = 0.607; Mann Whitney test; **Fig. 9**). The rise time of A-type currents was fast and independent of voltage in both LS and ES cells (**Fig. 9**). The decay time constants of A-type currents in LS cells were longer than those in ES cells at higher voltage commands (at +70 mV, LS cell, 37.58 ± 2.624, n = 9 vs. ES cell, 27.79 ± 1.691, n = 6; P < 0.01; Mann Whitney test**;** at +60 mV, LS cell, 35.03 ± 2.368, n = 9 vs. ES cell, 26.95 ± 1.684, n = 6; P = 0.036; Mann Whitney test**; Fig. 9**). On the other hand, no differences in the activation kinetics of delayed-rectifier K_v currents were observed between LS and ES cells (**Fig. 10**).

Subcellular localization of K_v1 channels

Given the fact that voltage-clamp experiments obtained from somatic nucleated patches did not show significant differences in functional expression of K_v channels

between ES and LS neurons, we thus assumed that localization of K_v1-like channels outside somatic areas may contribute to the distinct difference in firing patterns (Storm, 1988). To test this hypothesis, we investigated the subcellular localization of K_v channel proteins in CeL cells using immunohistochemistry (IHC). As shown in Fig. 11, the immunoreactivities of K_v1.1, K_v1.2, and K_v1.6 were detected at soma and processes of CeL cells. K_v1-like channels have been shown to be specifically expressed on axon initial segments (AISs) and contribute to the delayed firing phenotypes (Goldberg et al., 2008). We therefore performed double immunostaning for K_v1 channels and AIS marker Ank-G. The signal of K_v2 could be observed in putative jaxtaparanodal region (**Fig. 11D**), where K_v1 and K_v2 proteins are thought to specifically localize in. However, the image of double staining for K_v1 channels (green) and the AIS marker Ank-G (red) did not show any overlap between K_v1 channels and Ank-G, indicating that K_v1 channels are not segregated on the AISs of CeL cells.

Discussion

In this work, we divided CeL cells into two major types: LS cells and ES cells based on the firing patterns and other electrophysiological properties. The specific aim of this study is to characterize the ionic basis of the firing patterns of CeL neurons. Our finding suggests that the delayed firing of LS cells was mediated by K_v1-like current. Furthermore, we characterized the gating properties of K_v channels; however we did not observed the differences in the subtype composition and gating properties in K_v currents recorded from somatic patches. One possible explanation is that the subcellular distribution of K_v1-like channels is different between LS and ES cells. To probe this possibility, we attempted to detect any difference in subcellular localization of K_v1-like channel proteins of CeL cells using IHC; the result showed that $K_v1.1$, $K_v1.2$ and $K_v1.6$ proteins are expressed in the soma and processes of CeL neurons, but not in the AIS region.

Diversity of firing patterns in CeL neurons

Our study is consistent with previous studies (Martina et. al., 1999; Dumont et. al., 2002; Chieng et. al., 2006; Haubensak et al., 2010) that CeL neurons could be divided into two major classes based on their firing phenotypes in response to sustained depolarizing current injection. However, those studies did not further analyze the ionic mechanism of this diversity. In our study, we first made comprehensive characterization of electrophysiological properties of CeL cells. Next, we divided CeL neurons into two distinct, non-overlapping groups using the arbitrary cutoff latency (1.5 s). The classification made by the cutoff latency is almost consistent with the classification made by unbiased cluster analysis (Lien Lab unpublished data).

Mechanisms underlying different firing patterns of CeL neurons

Anatomical structure is known to contribute to neuronal firing pattern (Hodgkin and Huxley, 1952). We used Sholl analysis, a quantitative analysis to characterize the complexity of neuronal processes, to investigate the morphological properties of CeL neurons. According to the method (Sholl 1953), concentric circles were superimposed over the reconstructed cells with gradually increasing radius, and the cell body was placed in the center of the innermost circle. We managed to count the number of dendrite intersections and we could also measure the dendritic length via the software Neurolucida explorer. However, we did not find the difference of the morphological properties between LS and ES cells. Since there is no significant difference in dendritic structure between LS and ES cells, we excluded the influence of morphology on firing patterns and focused on the ionic basis under the diversity of firing patterns CeL neurons. In this study we used electrophysiology and immunohistochemistry to characterize the ionic mechanism underlying the variant firing pattern of CeL cells. We specifically focused on K_v channels. With the voltage sensor in structure, K_v channels could sense the change of membrane potentials, and modulate the potentials. Thus K_v channels are often considered to be involved in determining firing patterns of neurons.

Contribution of K_v1 channels in determining the spike delay

LS cells display the delayed firing upon long-lasting depolarization, which is likely mediated by the fast-activating, slow-inactivating D-type K^+ current mediated by voltage-gated K^+ type 1 (K_v1) channels, as D-type current activates rapidly and tends to keep the cell from depolarizing longer (Storm, 1988; Golding et al., 1999;Bekkers and Delaney, 2001; Dodson et al., 2002; Glazebrook et al., 2002; Guan et al., 2006; Miller et al., 2008; Goldberg et al., 2008). K_v1 subfamily of K_v channels is known to operate

at near-threshold potentials and would be responsible for action potential generation. Previous studies (Storm, 1988) showed that low-concentration, at which blocks D-type currents, 4-AP application could abolish the delayed spike latency of hippocampal neurons. We thus considered K_v1 channels to be the strong candidate for ionic basis underlying the variant firing pattern of CeL neurons. Here, we have shown that K_v1 channels blockers 4-AP and α-DTX abolished the subthreshold slow ramping depolarization and eliminated the delayed firing, converting the discharge and firing patterns of LS neurons from LS to ES cell-like. The reduction of spike delay upon applying low-concentration (30 μM) 4-AP and 100 nM α-DTX in LS cells indicates that LS cells apparently exhibit K_v1-like components, strongly suggesting that K_v1-like components play an important role in the spike latency of LS cells.

Properties of K_v currents

Considering K_v1 channels to be the strong candidate for the ionic basis underlying the delayed firing of LS neurons, we first checked the somatic K_v current properties via nucleated patches, the formation of a giant outside-out patch of somatic membrane surrounding the nucleus, providing larger number of channels than conventional outside-out patches (Sather et. al. 1991). The relatively large currents in nucleated patches also provide reliable measurement of conductance amplitude and density. Though there are limitations of nucleated patches experiment that the measurement were constricted in somatic channels, but with the sphere form of membrane, we could perform better voltage-clamp to measure the somatic K_v currents of CeL cells, diminishing the problem that the distal processes could not be voltage-clamped perfectly. We assumed that LS cells might express more K_v1 channels so that LS cells would exhibit longer spike latency. According to the results, blockage of K_v1 decreased

latency of the delayed firing, whereas the same concentration of 4-AP blockades in nucleated patches from LS and ES cells did not show difference, as 30 μM 4-AP had little effect on the K_v currents in nucleated patches from both CeL cells. This result implies that the differences of such K_v1-like component may not be present at soma. When we checked the properties of somatic K_v currents of CeL cells, we did not find the differences in the subtypes and activation curves, except for the decay time at test pulse of +70 mV. The results suggest that the somatic K_v channels of CeL neurons do not differ much in the subtypes, densities and the electrophysiological properties of activation and rise time of K_v currents. The results are not the same as we assumed that LS cells might express more K_v1 conductance. It is possible that the protocols to measure the K_v currents cannot tell the differences in activation of K_v channels between LS and ES cells, since the test pulse command voltages are much higher than the threshold for generation of action potentials.

Subcellular localization of K_v1 channels

As our voltage-clamp experiments suggested that differences of K_v1 channel expression may not be primarily on somatic region, we sought to determine the site of K_v1 channels localization. When it comes to the delayed generation of neuronal firing, the region where action potential generates were often considered. According to the published paper of Goldberg (2008), K_v1 channel subfamily proteins are rich in the AIS region of fast-spiking (FS) cells in the layer 2/3 barrel cortex, contributing the diversity of FS cells discharge patterns. It provides us with a direction to investigate the subcellular distribution of K_v1 channels. Since delayed firing of LS cells was blocked by low concentration 4-AP and α-DTX, we sought to investigate whether K_v1 proteins located at the AIS region. In the result of IHC experiment, we could observe

the immunoreactivity of K_v2 in putative jaxtaparanodal region (**Fig. 11**), where K_v1 and K_v2 proteins are thought to specifically localize in. However, we did not find the staining of K_v1 proteins colocalizing with Ank-G.

Although the result of IHC experiment was not as presumed that the low concentration 4-AP sensitive K_v channels are located at the AIS, we still could not exclude that expressions of those K_v channels on CeL cells vary from each other. We should note that there are some restrictions for K_v channels antibody and Ank-G colocalization, since the AIS region is also rich in anchored proteins of voltage-gated sodium channels (Wollner and Catterall, 1986; Boiko et. al., 2003), which would affect the detectability with an antibody, and the whole experimental procedure could affect the outcome. With some technical improvements, i.e. pepsin treatment before primary antibodies (Cattoretti et al., 1993; Wanatabe, 1998; Lorincz and Nusser, 2008) to improve detection sensitivity, we might get more specific immunoreactive signal for K_v channels and Ank-G proteins colocalization.

Another possibility resulting in different firing patterns of CeL cells

LS and ES cells also differ in their RMPs; the former have a more hyperpolarized RMP (-70.2 ± 0.5 mV) than that of the latter one (-66.4 ± 0.7 mV), which further indicate that the ES cells are more excitable compared to LS cells. Previous studies showed that the D-type current is largely inactivated when the RMP is positive to -65 mV (Storm, 1988), which is near the RMP of ES cells. The differences of RMP in LS and ES cells might also affect the activation of D-type currents and thus influence the spike initiation. The idea is that the D-type current of ES cells was inactivated before the depolarizing inputs were applied, so that it was unable to counteract inward Na^+

current. As a result, the action potential is generated earlier in ES cells. Collectively, a more depolarized RMP in ES cells is also likely to contribute to the firing patterns of CeL cells.

Physiological significance of K_v1 channels in CeL cells

The timing of action potential is crucial for neural coding. Here we showed that the spike timing of LS cells is modulated by K_v1-like currents. Some studies showed that K_v1-like channels participate in synaptic transmission (Storm, 1988; Kole et. al., 2007; Goldberg et. al., 2008). In addition, the K_v1-like current mediating the spike delay in LS cells is likely to determine the timing of spike generation during temporal integration of synaptic inputs.

Improvement of this study

Although this study showed some properties of K_v channels, there are some electrophysiological properties that we did not investigate. For instance, we did not demonstrate inactivation of K_v channels in CeL cells and therefore we could not ignore the role of this gating in determine the firing patterns. Inactivation of K_v channels could be a key factor in modulating the firing patterns. Since the D-type current takes up a long time (~20 seconds) to recover from inactivation (Storm, 1988), it would enable the cell to integrate the separate depolarizing inputs over several seconds.

References

Alle H., Kubota H., and Geiger J. R. (2011) Sparse but highly efficient K_v3 outpace BK_{Ca} channels in action potential repolarization at hippocampal mossy fiber boutons. J Neurosci. 31:8001-8012.

Amano T., Unal C. T., and Paré D. (2010) Synaptic correlates of fear extinction in the amygdale. Nat. Neurosci. 13(4): 489–494.

Amano T., Amir A., Goswami S., and Paré D. (2012) Morphology, PKCδ expression, and synaptic responsiveness of different types of rat central lateral amygdala neurons. J. Neurophysiol. 108:3196-3205.

Bekkers J. M., and Delaney A. J. (2001) Modulation of Excitability by α-Dendrotoxin-Sensitive Potassium Channels in Neocortical Pyramidal Neurons. The J.Neurosci.21:6553–6560.

Boiko T., Wart A., Caldwell J. H., Levinson S. R., Trimmer J. S., and Matthews G. (2003) Functional specialization of the axon initial segment by isoform-specific sodium channel targeting. J. Neurosci. 23(6):2306-2313.

Cattoretti, G., Pileri, S., Parravicini, C., Becker, M. H. G., Pogg, S., Bifulco, C., Key, G., D'Amato, L., Sabattini, E., Feudale, E., Reynolds, F., Gredes, J., and Rilke, F. (1993) Antigen unmasking of formalin-fixed, paraffin-embedded tissue sections. J. Pathol. 171:83-98.

Chieng B. C.H., McDonald J. C., and Osborne P. B. (2006) Characterization of neurons

in the rat central nucleus of the amygdale: cellular physiology, morphology, and opioid sensitivity. J. Comp. Neurol. 497:910-927.

Dodson P. D., Barker M. C., and Forsythe I. D. (2002) Two Heteromeric K_v1 Potassium Channels Differentially Regulate Action Potential Firing. J. Neurosci. 22(16):6953–6961.

Dumont E. C., Martina M., Samson R. D., Drolet G., and Pare D. (2002) Physiological properties of central amygdale neurons: species differences. Eur. J. Neurosci. 15:545-552.

Ehrlich I., Humeau Y., Grenier F., Ciocchi S., Herry C., and Luthi A. (2009) Amygdala inhibitory circuits and the control of fear memory. Neuron 62:757-771.

GlazebrookP. A., Ramirez A. N., Schild J. H., Shieh C. C., Doan T., Wible B. A., and Kunze D. L. (2002) Potassium channels $K_v1.1$, $K_v1.2$ and $K_v1.6$ influence excitability of rat visceral sensory neurons. J. Physio. 541:467–482.

Goldberg E. M., Clark B. D., Zagha E., Nahmani M., Erisir A., and Rudy B. (2008) K^+ channels at the axon initial segment dampen near-threshold excitability of neocortical fast-spiking GABAergic interneurons. Neuron 58:387-400.

Golding N. L., Jung H., Mickus T., and Spruston N. (1999) Dendritic calcium spike initiation and repolarization are controlled by distinct potassium channel subtypes in CA1pyramidal neurons. J. Neurosci. 19:8789–8798.

Guan D., Lee J. C. F., Tkatch T., Surmeier D. J., Armstrong W. E., and Foehring R. C. (2006) Expression and biophysical properties of K_v1 channels in supragranular neocortical pyramidal neurons. J. Physiol. 571:371–389.

Hamill O. P., Marty A., Neher E., Sakmann B., and Sigworth F. J. (1981) Improved patch-clamp techniques for high-resolution current recording from cells and cell-free membrane patches. Pflügers Arch 391:85-100.

Haubensak W., Kunwar P. S., Cai H.,Ciocchi S., Wall NR, Ponnusamy R., Biag J., Dong H. W., Deisseroth K., Callaway E. M., Fanselow M. S., Lüthi A., and Anderson D. J. (2010) Genetic dissection of an amygdala microcircuit that gates conditioned fear. Nature 468:270-276.

Hu H., Martina M., and Jonas P. (2010) Dendritic mechanisms underlying rapid synaptic activation of fast-spiking hippocampal interneurons. Science 327:52-58.

Hodgkin A. L., and Huxley A. F. (1952) A quantitative description of membrane current and its application to conduction and excitation in nerve. J. Physio. 117:500-544.

Johansen J. P., Cain C. K., Ostroff L. E., and LeDoux J. E. (2011) Molecular mechanisms of fear learning and memory. Cell 147(3): 509–524.

Kirchheim F., Tinnes S., Haas C. A., Stegen M., and Wolfart J. (2013) Regulation of action potential delays via voltage-gated potassium $K_v1.1$ channels in dentate granule cells during hippocampal epilepsy. Front Cell Neurosci. 7:248.

Kole M. H., Letzkus J. J., and Stuart, G. J. (2007) Axon initial segment K_v1 channels control action potential waveform and synaptic efficacy. Neuron 16:633-647.

Li H., Penzo M. A., Taniguchi H., Kopec C. D., Huang Z. J., and Li B. (2013) Experience-dependent modification of a central amygdala fear circuit. Nat. Neurosci. 16:332-229.

Lien C. C., and Jonas P. (2003) K_v3 potassium conductance is necessary and kinetically optimized for high-frequency action potential generation in hippocampal interneurons. J. Neurosci. 23:2058-2068.

Lopez de Armentia M., and Sah P. (2004) Firing properties and connectivity of neurons in the rat lateral central nucleus of the amygdala. J. Neurophysiol. 92:1285-1294.

Lorincz A., and Nusser Z. (2008) Specificity of immunoreactions: the importance of testing specificity in each method J. Neurosci. 28(37):9083-9086.

Mainen Z. F., and Sejnowski T. J. (1996) Influence of dendritic structure on firing pattern in model neocortical neurons. Nature 382:363-366.

Martina M., Royer S., and Paré D. (1999) Physiological properties of central medial and central lateral amygdala neurons. J. Neurophysiol. 82:1843-54.

Myatt D. R., Hadlington T., Ascoli G. A., Nasuto S. J. (2012) Neuromanic– from semi-manual to semi-automantic reconstruction of neuron morphology. Front Neuronoinform 6:4.

Miller M. N., Okaty B. W., and Nelson S. B. (2008) Region-specific spike frequency acceleration in Layer 5 pyramidal neurons mediated by K_v1 subunits. J. Neurosci. 28:13716–13726.

Pitkänen A., Savander V., and LeDoux J. E. (1997) Organization of intra-amygdaloid circuitries in the rat: an emerging framework for understanding functions of the amygdala. Trends Neurosci. 20:517-523.

Sather W., Dieudonne S., MacDonald J. F., and Ascher P. (1991) Activation and desensitization of N-methyl-D-aspartate receptors in nucleated outside-out patches from mouse neurons. J. Physio. 450:643-672.

Sholl D. A. (1953) Dendritic organization in the neurons of the visual and motor cortices of the cat. J. Anat. 87:387-406.

Storm J. F. (1988) Temporal integration by a slowly inactivating K^+ current in hippocampal neurons. Nature 336:379-381.

Viviani D., Charlet A., van den Burg E., Robinet C., Hurni N., Abatis M., Magara F., and Stoop R. (2011) Oxytocin selectively gates fear responses through distinct outputs from the central amygdala. Science 333:104-107.

Watanabe M., Fukaya M., Sakimura K., Manabe T., Mishina M., and Inoue Y. (1998) Selective scarcity of NMDA receptor channel subunits in the stratum lucidum (mossy fibre-recipient layer) of the mouse hippocampal CA3 subfield. Eur. J. Nurosci. 10:478-487.

Wollner D. A., and Catterall W. A. (1986) Localization of sodium channels in axon hillocks and initial segments of retinal ganglion cells. Proc. Natl. Acad. Sci.83:8424–8428.

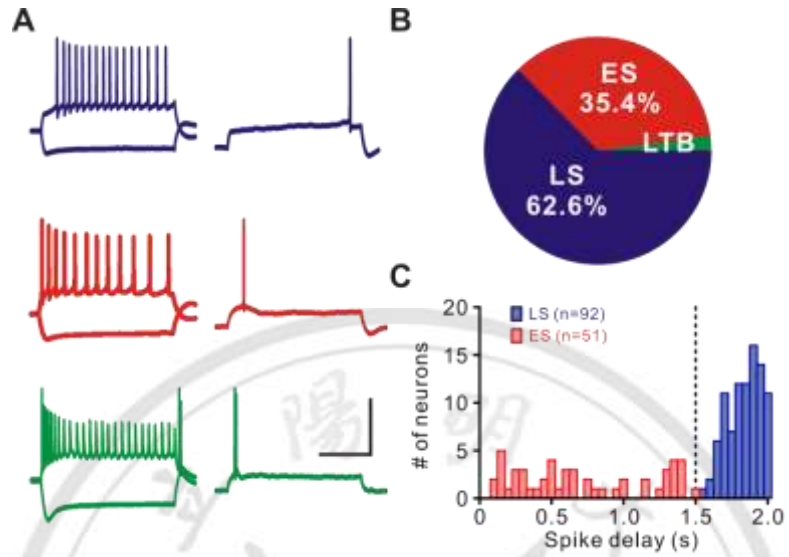

Figure 1. Firing properties of CeL cells

A: Firing patterns of CeL neurons. Left: voltage responses to 100 pA and -50 pA current pulse injection. Right: voltage responses to the rheobase, the minimum current required for a given neuron to generate action potentials. Blue traces represent LS cells, red traces represent ES cells, and green traces represent LTB cells. Scale bars: 80 mV; 400 ms.

B: Proportions of CeL neurons. The majority of CeL neurons are LS cell (62.6%) and ES cell (35.4%). There is a small subset of neurons (~3%), called LTB cells.

C: Histogram of spike delay of CeL neurons. LS, n = 92; ES, n = 51. Bin size, 5ms; vertical dashed line denotes 1.5 second after current injection.

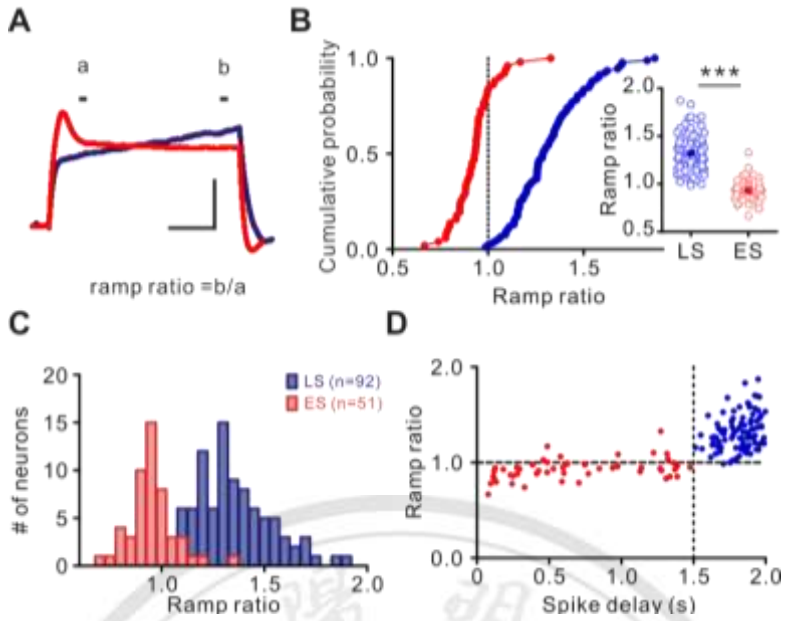

Figure 2. Subthreshold ramping phenotype of LS cells

A: Schema showing how the ramp ratio is measured. Traces show the voltage responses to the current injection which is 1 pA smaller than the rheobase for the cells. The blue trace represents the voltage change of a LS cell, which is featured by the ramping depolarization. The ramp ratio is defined as the ratio of the average voltage responses within indicated periods a and b. Period a represents the time period of 200-250 ms after the current injection onset, while period b is 150-200 ms before the current injection ended. Scale bars: 50 mV; 1 sec.

B: Left, cumulative plot of ramp ratio of CeL neurons; Right, scatter plot of ramp ratio. Note that LS cells have larger value of ramp ratio compared to ES cells (***$p < 0.0001$).

C: Histogram of ramp ratio of CeL neurons. Bin size, 0.05 sec.

D: Plot of ramp ratio versus spike delay of CeL neurons. Blue dots represent LS cells. Most LS cells have the value of ramp ratio larger than 1.0 and show spike delay longer than 1.5 s; red dots represent ES cells, with smaller values.

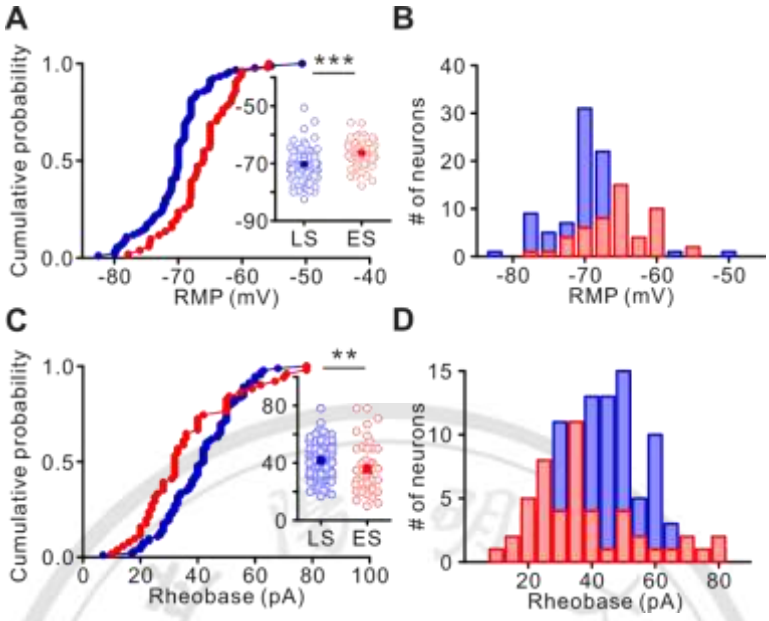

Figure 3. Intrinsic properties of CeL cells

A: Cumulative plot and quantification of RMP of CeL neurons. LS cells show more hyperpolarized RMP (-70.47 ± 6.46 mV, n = 92) than that of ES cells (-65.93 ± 6.29 mV, n = 51).

B: Histogram of RMP of CeL neurons. Bin size: 2.5 mV.

C: Cumulative plot and quantification of rheobase of CeL neurons. LS cells have larger value (41.79 ± 1.3 pA, n = 92) of rheobase, while ES cells require smaller current (35.79 ± 2.48 pA, n = 51) to generate action potentials.

D: Histogram of rheobase of CeL neurons. Bin size: 5 pA.

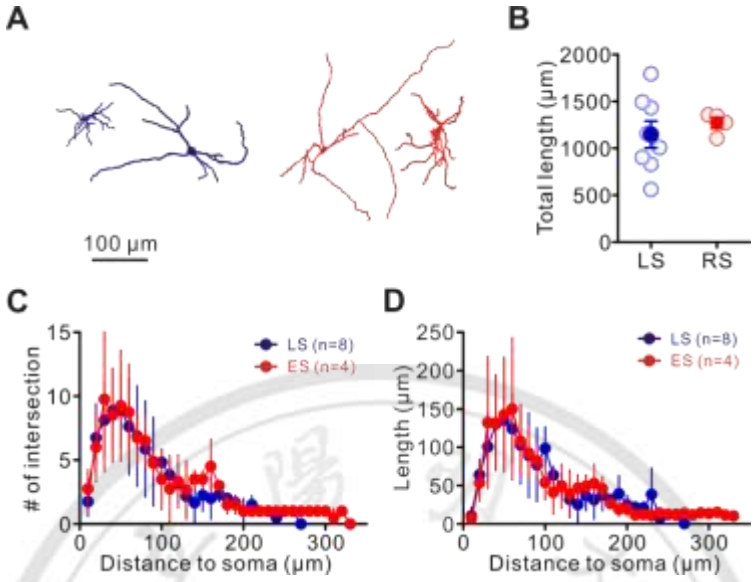

Figure 4. Morphological analysis

A: Reconstructed CeL neurons, blue color for LS cells, and red color for ES cells. Scale bar: 100 µm.

B: Comparing the total length between LS and ES cells.

C: Sholl analysis of CeL neurons. Number of intersections plot against distance to soma.

D: Sholl analysis of CeL neurons. Length plot against distance to soma.

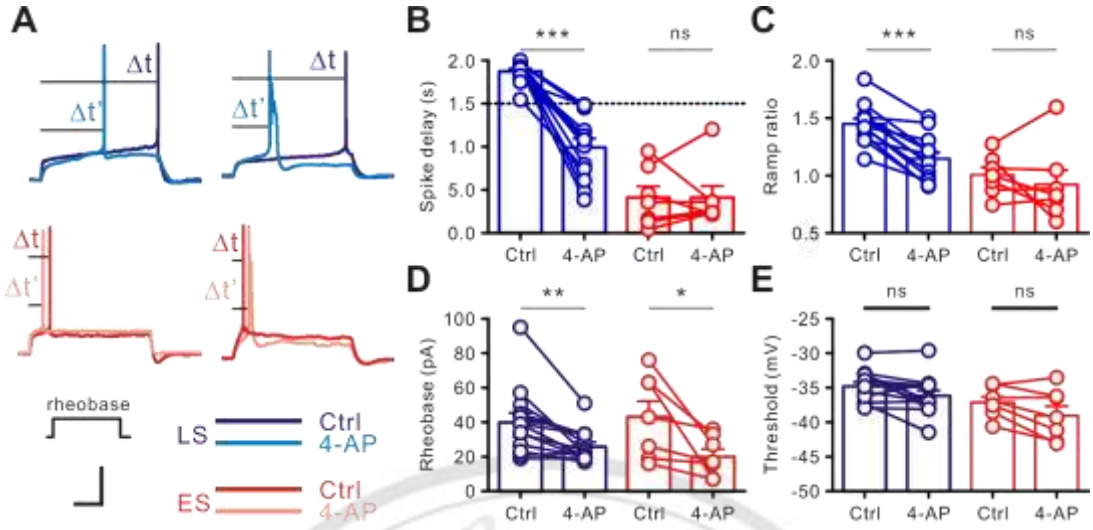

Figure 5. Effect of K_v channel blocker 4-AP on firing properties

A: Traces represent voltage responses of CeL cells to the 2-second current injection at rheobase of the given neurons, showing shortened spike delay by 4-AP. Scale bars: 40 mV; 500 ms

B: Summary of 4-AP effect on spike delay. Application of 30 μM 4-AP abolishes the delayed firing of LS cells, while has little effect on ES cells.

C: Summary of 4-AP effect on ramp ratio. Application of 30 μM 4-AP eliminates the ramping depolarizing phenotype, but does not do much to ES cells.

D: Summary of 4-AP effect on rheobase. The rheobases of both LS and ES cells are reduced by 30 μM 4-AP.

E: Summary of 4-AP effect on spike threshold. ns, not significant.

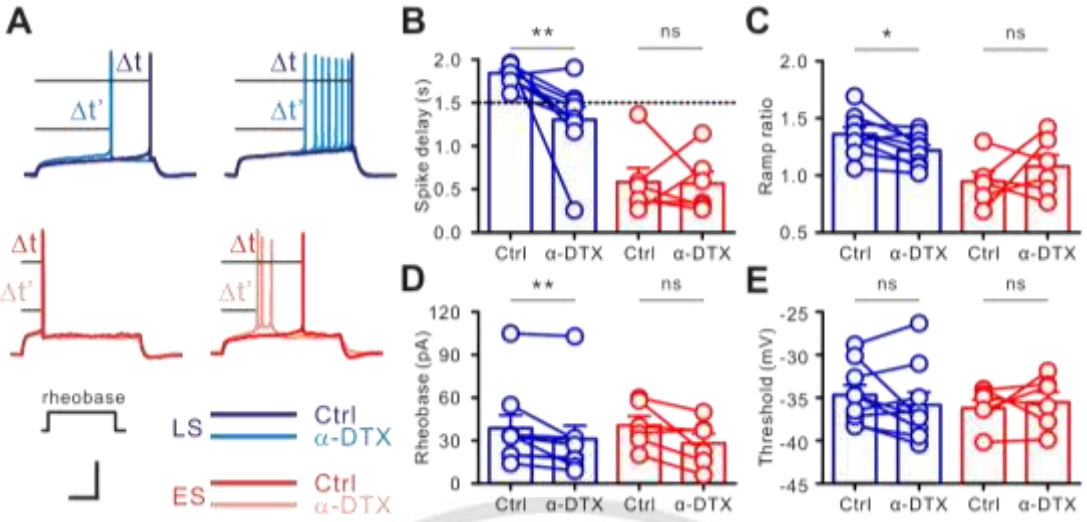

Figure 6. Effect of K_v channel blocker α-DTX on firing properties

A: Traces represent voltage responses of CeL cells to the 2-second current injection at rheobase of the given neurons, showing shortened spike delay by α-DTX. Scale bars: 40 mV; 500 ms.

B: Summary of α-DTX effect on spike delay. Application of 100 nM α-DTX could reduce the spike delay of LS cells, but there's no significant effect on ES cells.

C: Summary of α-DTX effect on ramp ratio. Application of 100 nM α-DTX eliminates the ramping depolarizing phenotype, but does not do much to ES cells.

D: Summary of α-DTX effect on rheobase. The rheobases of both LS and ES cells are reduced by 100 nM α-DTX.

E: Summary of α-DTX effect on spike threshold. Spike thresholds are not influenced much in both LS and ES cells.

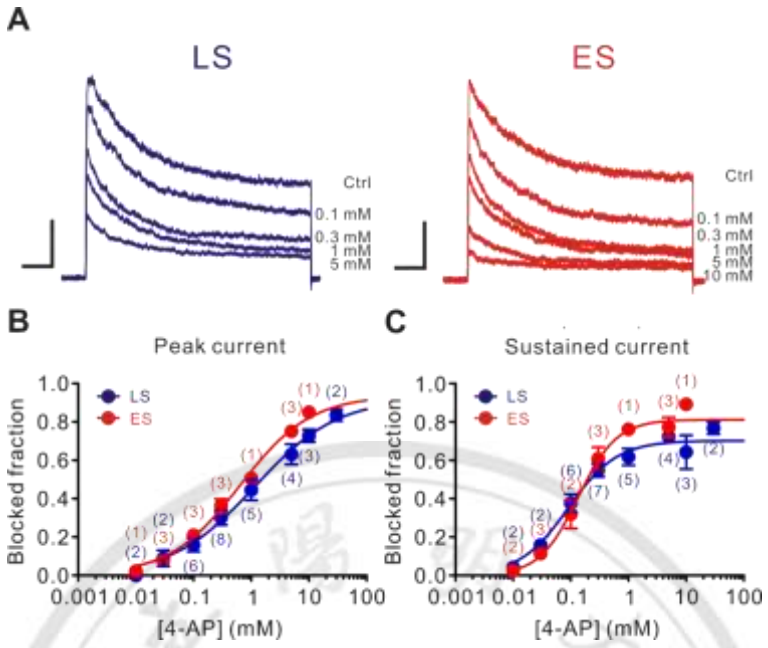

Figure 7. Dose response for 4-AP

A: Traces show currents evoked in nucleated patches from LS and ES cells. The current amplitudes are inhibited by different 4-AP concentrations, showing 4-AP blockage. Scale bars: 100 pA; 20 ms.

B: Inhibition of peak K^+ current by 4-AP, plot against 4-AP concentration.

C: Inhibition of sustained K^+ current by 4-AP, plot against 4-AP concentration.

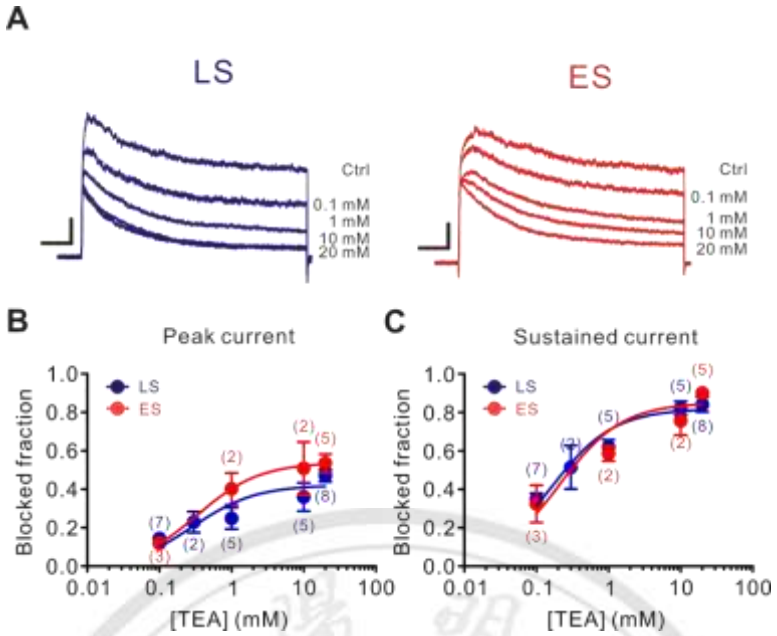

Figure 8. Dose response for TEA

A: Traces show currents evoked in nucleated patches from LS and ES cells. The current amplitudes are reduced by TEA variant TEA concentration, showing TEA blockage. Scale bars: 100pA; 20 ms.

B: Inhibition of peak K^+ current by TEA, plot against TEA concentration.

C: Inhibition of sustained K^+ current by TEA, plot against TEA concentration.

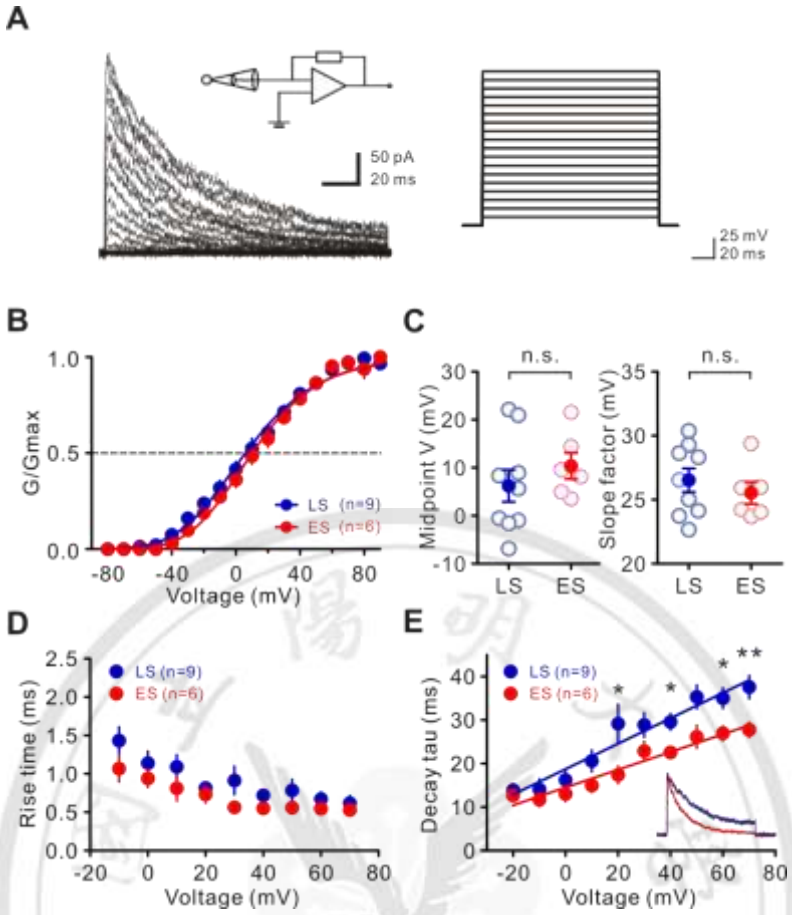

Figure 9. Properties of A-type K_v current

A: Traces of K^+ currents evoked in a nucleated patch from a LS cell in the presence of 20 mM TEA. The remaining TEA-insensitive currents show fast-activating and inactivating properties.

B: Activation curves of A-type K^+ current from LS and ES patches. Data points were fitted with Boltzmann functions raised to the fourth power.

C: Summary of A-type K^+ current midpoint potential and slope factor.

D: 20-80% rise time of A-type K^+ current from LS and ES patches, plotted against test pulse voltage.

E: Decay tau of A-type K^+ current from LS and ES patches, plotted against test pulse voltage. Traces show normalized A-type K^+ current at +70 mV.

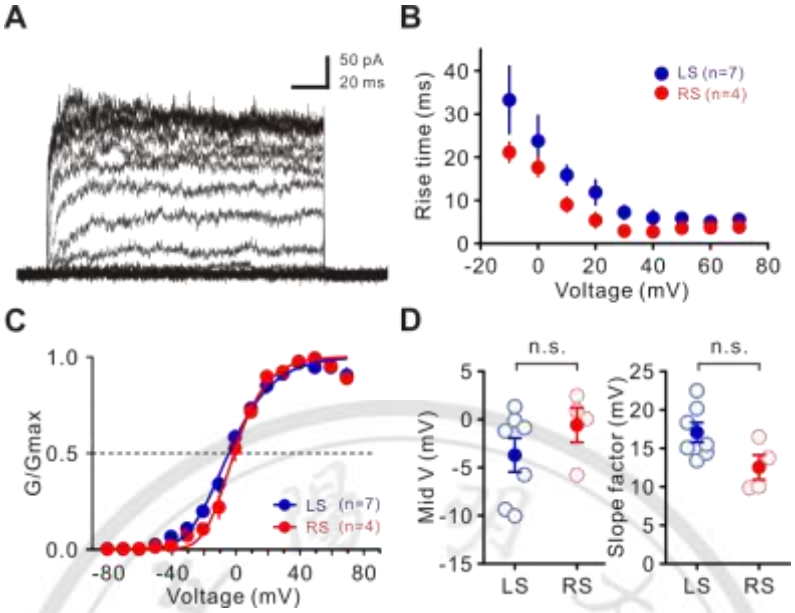

Figure 10. Delayed-rectifier K_v current properties

A: Traces of K^+ currents obtained in subtraction ($I_{control} - I_{20\ mM\ TEA}$) in a nucleated patch from a LS cell.

B: 20-80% rise time of delayed-rectifier K^+ current LS and ES patches, plotted against test pulse voltage.

C: Activation curve of delayed-rectifier K^+ current for LS and ES patches. Data points were fitted with Boltzmann functions raised to the fourth power.

D: Summary of delayed-rectifier K^+ current midpoint potential and slope factor.

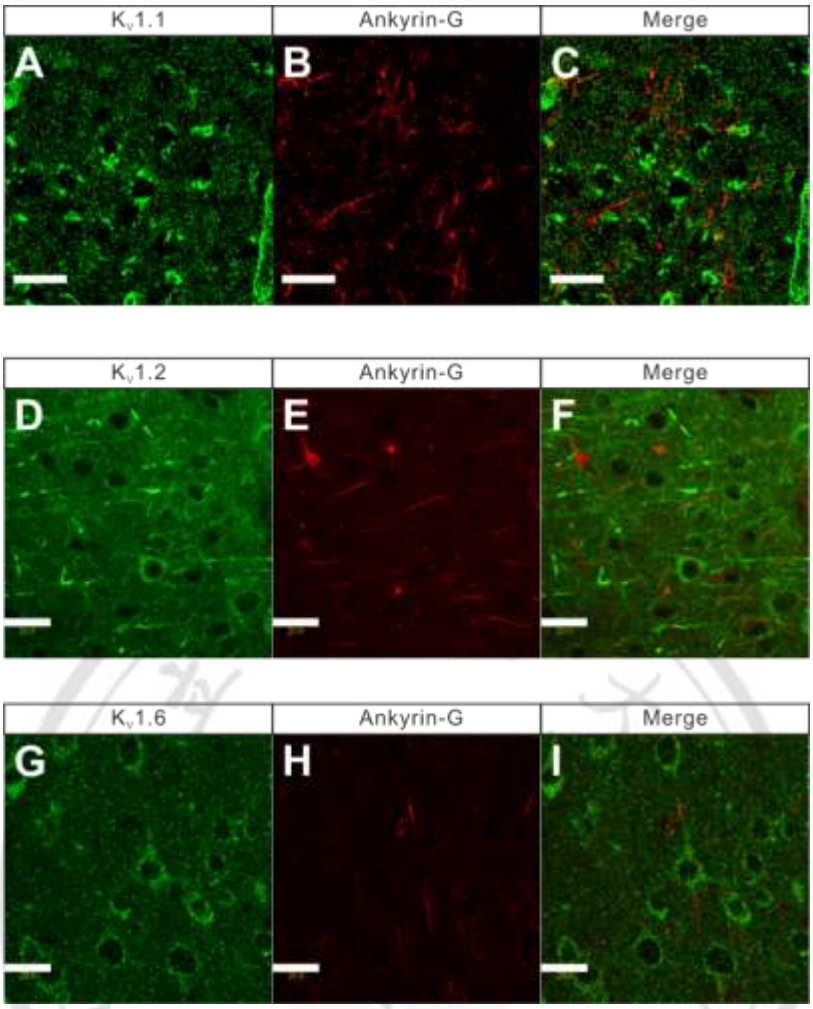

Figure 11. Colocalization of K_v channels and Ank-G

A: The K_v1.1 immunoreactive cells in CeL region.

B: Immunostaining of the same region in (A) for Ank-G, denotes the AIS region.

C: Superimpose of (A) and (B).

D: The K_v1.2 immunoreactive cells in CeL region.

E: Immunostaining of the same region in (D) for Ank-G.

F: Superimpose of (D) and (E).

G: The K_v1.6 immunoreactive cells in CeL region.

H: Immunostaining of the same region in (G) for Ank-G.

I: Superimpose of (G) and (H).

Scale bars, 20 μm.